

# Synthesis and gas-sensing properties of nano- and meso-porous MoO<sub>3</sub>-doped SnO<sub>2</sub>

Azam Anaraki Firooz<sup>1,2</sup>, Takeo Hyodo<sup>1,\*</sup>, Ali Reza Mahjoub<sup>2</sup>, Abbas Ali Khodadadi<sup>3</sup>, Yasuhiro Shimizu<sup>1</sup>

<sup>1</sup>Department of Materials Science and Engineering, Faculty of Engineering, Nagasaki

University, 1-14 Bunkyo-machi, Nagasaki 852-8521, Japan

<sup>2</sup>Department of Chemistry, Tarbiat Modares University, 14115-175, Tehran, Iran

<sup>3</sup>School of Chemical Engineering, University of Tehran, 11155-4563 Tehran, Iran

\*Corresponding author:

*E-mail address:* hyodo@nagasaki-u.ac.jp (T. Hyodo).

## Abstract

Nano- and meso-porous SnO<sub>2</sub> powders doped with and without 1~10 wt% MoO<sub>3</sub> have been synthesized by an ultrasonic spray-pyrolysis method employing a precursor aqueous solution containing tin (IV) chloride pentahydrate (SnCl<sub>4</sub>·5H<sub>2</sub>O), ammonium heptamolybdate and polymethylmethacrylate (PMMA) microspheres as a template, and the effects of MoO<sub>3</sub>-doping and the addition of PMMA microspheres on the structural, morphological and gas-sensing properties of SnO<sub>2</sub> were investigated in this study. It is confirmed that control of the amounts of PMMA microspheres in the precursor solution was effective in realizing well-developed nano- and meso-porous structures of SnO<sub>2</sub> by X-ray diffraction analysis, scanning electron microscopy, transmission electron microscopy, X-ray photoelectron spectroscopy, and the measurement of specific surface area and pore size distribution using a N<sub>2</sub> adsorption isotherm. Gas-sensing properties of their thick films (about 50 μm thick), which were fabricated by screen-printing to various gases (NO<sub>2</sub>, C<sub>2</sub>H<sub>5</sub>OH and H<sub>2</sub>) were tested in ambient air. The doped thick films showed a high response and selectivity to 5 ppm NO<sub>2</sub> gas in the case of 10 wt% MoO<sub>3</sub>-doping in both nano- and meso-porous structures of SnO<sub>2</sub>. We observed that the presence of Mo species in SnO<sub>2</sub> lattice can improve the sensor response and selectivity towards NO<sub>2</sub> gas. The effect of the MoO<sub>3</sub>-doping on the sensing characteristics of these films towards NO<sub>2</sub> was discussed.

**KEYWORDS:** SnO<sub>2</sub>; porous structure; MoO<sub>3</sub>; gas sensor; ultrasonic spray-pyrolysis

## 1. Introduction

In recent years, much effort has been devoted to the synthesis of nanostructured tin oxide with specific morphology because of their novel optical, electrical and catalytic properties [1-3]. There are two ways that can improve these properties of SnO<sub>2</sub>. One is doping of a metal or metal oxide into SnO<sub>2</sub> structure, which would induce a significant effect on its physical and chemical properties [4, 5]. Another one is to synthesize nanostructured SnO<sub>2</sub>, which would contribute to the achievement of a high specific surface area and quantum size effects [6, 7]. The strict control of novel nano/microstructures with well-defined shape and doped with a metal or metal oxide may open new opportunities for exploring unique physical and chemical properties and more potential applications [8, 9]. Therefore, development of morphologically controllable synthesis of SnO<sub>2</sub> nano/microstructures doped with a metal or metal oxide is urgently important to answer the demand for exploring the potentials of SnO<sub>2</sub> [10]. Nowadays, the addition of MoO<sub>3</sub> to SnO<sub>2</sub> has been devoted to obtain good morphological SnO<sub>2</sub>/MoO<sub>3</sub> nanostructures in order to improve the sensing characteristics. MoO<sub>3</sub> is n-type semiconductor that can change the acidity performances of SnO<sub>2</sub> surfaces against reactivity with different gases [11, 12]. The introduction of

MoO<sub>3</sub> reduces the electrical conductivity of SnO<sub>2</sub> by two orders of magnitude in air, which may be due to the transfer of electrons trapped at oxygen vacancies to Mo<sup>6+</sup> [13].

Generally, it is difficult to control the size and morphology of the oxide composites, which have important influence on their physical and chemical properties. In order to improve selectivity and sensor response to a particular target gas, we prepared a series of SnO<sub>2</sub> doped with and without MoO<sub>3</sub> (0~10 wt%) by ultrasonic spray-pyrolysis of the precursor mist and also performed a detailed analysis of the morphology and chemical states by scanning electron microscopy (SEM), transmission electron microscopy (TEM) and X-ray photoemission spectroscopy (XPS), to explain the changes in the sensing characteristics.

## **2. Experimental**

In this paper, we synthesized two different structures, nano- and meso-porous SnO<sub>2</sub> doped with and without MoO<sub>3</sub> by ultrasonic spray-pyrolysis. SnCl<sub>4</sub>·5H<sub>2</sub>O and (NH<sub>4</sub>)<sub>6</sub>Mo<sub>7</sub>O<sub>24</sub> were used as a raw material of a host (SnO<sub>2</sub>) and a dopant, respectively, and a PMMA microsphere was added as a template in the precursor solution.

Porous SnO<sub>2</sub> doped with and without MoO<sub>3</sub> (1, 5, and 10 wt%) were synthesized via ultrasonic spray-pyrolysis (USP) with a specially designed mist-supply to prepare a porous SnO<sub>2</sub> powder in an electric furnace heated at 1100°C [14]. 0.005 mol SnCl<sub>4</sub>·5H<sub>2</sub>O and (NH<sub>4</sub>)<sub>6</sub>Mo<sub>7</sub>O<sub>24</sub> were dissolved in 50 mL H<sub>2</sub>O separately. Mixing of these solutions was done using a magnetic stirrer for 3 h, followed by addition of 3 or 5 g PMMA microspheres (Soken Chem. & Eng. Co., Ltd., 150 nm in diameter). The porous SnO<sub>2</sub> doped with and without MoO<sub>3</sub> obtained were denoted as pr-*m*MoO<sub>3</sub>-SnO<sub>2</sub>(*n*) or pr-SnO<sub>2</sub>(*n*) (*n*: the amount of PMMA microspheres in the precursor solution (3 and 5 g), *m*: the amount of Mo addition (1, 5 and 10 wt%), respectively. Using 3 and 5 g PMMA microspheres caused to get nano- and meso-porous structures, respectively, as will be confirmed later. The morphologies of pr-SnO<sub>2</sub>(*n*) and pr-*m*MoO<sub>3</sub>-SnO<sub>2</sub>(*n*) powders were observed by SEM (JEOL Ltd., JSM-7500F) and TEM (JEOL Ltd., JEM2010-HT). The specific surface area and pore size distribution were measured by BET and BJH methods using a N<sub>2</sub> adsorption isotherm (Micromeritics, Tristar3000). Crystal phase and mesoporous structure of the samples were characterized by X-ray diffraction analysis (XRD; Rigaku Corp., RINT2200) using CuKα radiation (40 kV, 40 mA). The change in chemical states was

measured with X-ray photoelectron spectroscopy (XPS, Kratos Analytical Ltd., AXIS-ULTRA DLD).

Thick film sensors (about 50  $\mu\text{m}$  thick) were fabricated by screen-printing of  $\text{pr-SnO}_2(n)$  or  $\text{pr-}m\text{MoO}_3\text{-SnO}_2(n)$  powders on alumina substrates equipped with a pair of interdigitated Pt electrodes (the distance between Pt electrodes is ca. 200  $\mu\text{m}$ .), followed by calcination at 400°C for 5 h. Gas responses of these sensors were measured to 5 ppm  $\text{NO}_2$  balanced with air in a flow apparatus at 250–400°C in order to find out the optimum operating temperature, and these sensors were stabilized for 5 h at the working temperature before exposure to the target gas. Sensor response was defined as the ratio ( $R_a/R_g$ ) of sensor resistance in air ( $R_a$ ) to that in gas balanced with air ( $R_g$ ). To investigate the selectivity of the sensors to  $\text{NO}_2$  gas, the responses to other reducing gases such as  $\text{C}_2\text{H}_5\text{OH}$  (100 ppm) and  $\text{H}_2$  (1000 ppm) were also examined and compared with those to  $\text{NO}_2$  gas.

### **3. Results and discussions**

#### **3.1 Characterization of $\text{pr-SnO}_2(n)$ and $\text{pr-}m\text{MoO}_3\text{-SnO}_2(n)$ powders**

Figure 1 shows the X-ray diffraction patterns of all samples. All the prominent peaks in the pattern corresponded to the rutile structure of SnO<sub>2</sub>, which is indexed on the basis of JCPDS file No. 41-1445. No peaks corresponding to MoO<sub>3</sub> were observed; indicating that MoO<sub>3</sub> may incorporate into the tin oxide lattice. The full width at half maximum (FWHM) slightly changed with the addition of MoO<sub>3</sub>. The data showed that FWHMs of pr-*m*MoO<sub>3</sub>-SnO<sub>2</sub>(3) and pr-*m*MoO<sub>3</sub>-SnO<sub>2</sub>(5) tended to increase and decrease with the additive amounts of MoO<sub>3</sub>, respectively. Also, the variations in the lattice parameters were shown in Figure 1. It is seen that on doping of MoO<sub>3</sub> in pr-SnO<sub>2</sub>(3) and pr-SnO<sub>2</sub>(5) a marginal decrease and increase in the ‘*a*’ parameters is observed in all the concentrations, respectively, while ‘*c*’ (*c* = 3.195 Å) remains almost unchanged in all samples. These parameters were in good agreement with crystallite size.

Figure 2 shows SEM photographs of all samples. The microstructural morphology of all samples reflected the shape of submicron-size PMMA microspheres (d: 150 nm), but the diameter of the macropores was about 50–100 nm. It was smaller than the PMMA diameter, probably due to the slower pyrolysis rate of PMMA than that of tin chloride and shrinkage by the growth of SnO<sub>2</sub> crystallites [14]. In addition, the

macropores of  $\text{pr-SnO}_2(3)$  and  $\text{pr-}m\text{MoO}_3\text{-SnO}_2(3)$  powders were hollow spheres, while those of  $\text{pr-SnO}_2(5)$  and  $\text{pr-}m\text{MoO}_3\text{-SnO}_2(5)$  powders were largely destroyed (the pores were not spheres). It seemed that the presence of many PMMA microspheres led to deformation of these pores. Figure 3 shows schematically the formation mechanism of these samples. In case of  $\text{pr-}m\text{MoO}_3\text{-SnO}_2(3)$  powders, PMMA microspheres were relatively dispersed in the droplets of precursor solution, because the amount of PMMA microspheres was small. Therefore, the spherical pores reflecting the shape of PMMA microspheres remained uniformly and the oxide walls were formed stably among these pores, even after burning of PMMA and decomposition of the precursors, as shown in Figs. 2 (a)-(d). In case of  $\text{pr-}m\text{MoO}_3\text{-SnO}_2(5)$  powders, on the other hand, the distances among the PMMA microspheres reduced by an increase of their numbers in the droplets, because the amount of oxide precursors was much less than that of PMMA microspheres in the droplets. Therefore, the oxide walls with mechanical stability could not be formed among the pores during the burning, and thus the obtained pores and oxide walls likely destroyed in the  $\text{pr-}m\text{MoO}_3\text{-SnO}_2(5)$  powders.

Figures 4 and 5 show pore size distribution and specific surface area (SSA) of all samples. As shown in Fig. 4, the surface area and the amount of nanopores with a size



of 2-4 nm in diameter of *pr-m*MoO<sub>3</sub>-SnO<sub>2</sub>(3) powders increased with an increase in the amount of MoO<sub>3</sub>. In contrast, as shown in Fig. 5, the addition of 5 g PMMA microspheres in the precursor solution caused to decrease the surface area with an increase in the amount of MoO<sub>3</sub> in *pr-m*MoO<sub>3</sub>-SnO<sub>2</sub>(5). Also, it showed that the amount of mesopores of ca. 30 nm in diameter decreased with an increase in the amount of MoO<sub>3</sub> with a slight increase in nanopores of ca. 2-3 nm in diameter. These results emphasize that nanopores of less than about 4 nm reflect the spaces formed among crystallites, while mesopores of about 30 nm seem to correspond to the spaces formed among crystallite agglomerates [14]. Considering the amount of addition of PMMA microspheres and the morphology of samples, it seems that all the molybdenum-components should be well-dissolved in SnCl<sub>4</sub> solutions. During the firing at elevated temperatures, OH<sup>-</sup> and NH<sub>4</sub><sup>+</sup> removed as H<sub>2</sub>O and NH<sub>3</sub>, and MoO<sub>3</sub> doped SnO<sub>2</sub> was formed. Because, Mo<sup>6+</sup> ions with an atomic radius of 0.42 Å can easily occupy the tin lattice sites (atomic radius of Sn<sup>4+</sup> = 0.68 Å). But addition of 5 g PMMA microspheres may accelerate segregation of MoO<sub>3</sub> from the SnO<sub>2</sub> lattice. So, MoO<sub>3</sub> may be separately formed. The proposed mechanism was confirmed by EDX, SAED and TEM observations of *pr-10*MoO<sub>3</sub>-SnO<sub>2</sub>(3), *pr-10*MoO<sub>3</sub>-SnO<sub>2</sub>(5) and *pr-SnO*<sub>2</sub>(5). Thus,

the introduction of MoO<sub>3</sub> in the lattice of SnO<sub>2</sub> resulted in a decrease of the size of SnO<sub>2</sub> nanoparticles and an increase the surface area.

Figures 6, 7 and 8 show TEM images of pr-SnO<sub>2</sub>(5), pr-10MoO<sub>3</sub>-SnO<sub>2</sub>(3) and pr-10MoO<sub>3</sub>-SnO<sub>2</sub>(5), respectively, together with their SAED patterns. These figures indicated that the oxide walls consisted of very fine particles. The size of nanoparticles of pr-10MoO<sub>3</sub>-SnO<sub>2</sub>(3) is smaller than those of other two samples, and the spaces among their crystallites was in good agreement with the size of nanopores of the pore size distribution as shown in Figs. 4 and 5. Interestingly, large particles (sizes above 25 nm) cohabited among the small nanoparticles of pr-10MoO<sub>3</sub>-SnO<sub>2</sub>(5) (see Fig. 8a). The EDX results showed that they were related to pure MoO<sub>3</sub> phase, while the data is not show here. This is perfectly in agreement with the BET analytical results. Namely, it indicates that the addition of large amount of PMMA microspheres (5 g) can accelerate segregation of MoO<sub>3</sub> from the SnO<sub>2</sub> lattice and produces pure MoO<sub>3</sub> agglomerates.

SAED patterns of these 3 samples (Figs. 6(b), 7(b) and 8(b)) confirmed the well crystallization structure of their SnO<sub>2</sub> nanoparticles. The selected area exhibited distinctly three diffraction rings, which corresponded to the (1 1 0), (1 0 1) and (2 1 1) planes of the tetragonal-phase SnO<sub>2</sub> with rutile structure, respectively. With a careful

observation of SAED pattern in Fig. 8(b), many bright spots could be indexed as a  $\text{MoO}_3$  phase of large particles (above 25 nm), while faint rings were indexed as a cassiterite  $\text{SnO}_2$  phase of small nanoparticles (6-10 nm).

On the other hand, the prepared products were polycrystalline as illustrated by high-resolution (HR) TEM observations (Figs. 6(c), 7(c) and 8(c)) consist of very fine particles. The spacing of the lattice fringes for  $\text{pr-}10\text{MoO}_3\text{-SnO}_2(n)$  ( $n=3$ , and 5) and  $\text{pr-SnO}_2(5)$  was found to be 3.35 and 2.21 Å, respectively and these planes are best indexed as (1 1 0) and (2 1 0) of rutile  $\text{SnO}_2$ , respectively. Also, as shown in Fig. 8(c), the HRTEM image of  $\text{MoO}_3$  particles revealed the clear lattice fringes illustrate the high crystallization of these particles. Therefore,  $\text{MoO}_3$  phase which is stable up to 400°C [15] existed in the  $\text{pr-}10\text{MoO}_3\text{-SnO}_2(5)$  even after firing at 1100°C.

Figures 9 and 10 show XPS spectra of  $\text{Sn}3d$  and  $\text{Mo}3d$  of  $\text{pr-SnO}_2(5)$  and  $\text{pr-}10\text{MoO}_3\text{-SnO}_2(n)$  ( $n = 3, 5$ ). The  $\text{pr-SnO}_2(5)$  exhibited two  $\text{Sn}3d$  peaks ( $3d_{5/2}$  at 486.6 eV and  $3d_{3/2}$  at 494.8 eV) and single peak of  $\text{O}1s$  at 530.4 eV (not shown here), which corresponded to the values of the lattice tin and lattice oxygen of general  $\text{SnO}_2$ , respectively [16]. The XPS spectra of  $\text{Sn}3d$  of  $\text{pr-}10\text{MoO}_3\text{-SnO}_2(5)$  showed slightly lower binding energy than those of  $\text{pr-SnO}_2(5)$ . Interestingly, XPS spectra of  $\text{Sn}3d$  of

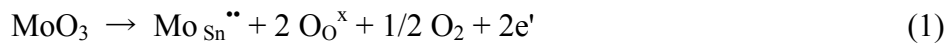
pr-10MoO<sub>3</sub>-SnO<sub>2</sub>(3) showed relatively higher binding energy. These shifts may be explained by the presence of many Mo cations in SnO<sub>2</sub> lattices, creating an oxygen-rich surface layer on this sample [17]. On the other hand, the pattern observed for MoO<sub>3</sub> was due to the spin orbit splitting of Mo 3*d* levels giving rise to Mo 3*d*<sub>5/2</sub> and Mo 3*d*<sub>3/2</sub> levels with an energy separation of 3.2 eV [18]. Binding energy of Mo 3*d*<sub>3/2</sub> and Mo 3*d*<sub>5/2</sub> levels for pr-10MoO<sub>3</sub>-SnO<sub>2</sub>(3) were observed at 233.3 eV and 236.5 eV, respectively. The values were close to the reported literatures [19] and confirmed that Mo was present mainly in +6 oxidation state. However, XPS spectra of Mo3*d*<sub>5/2</sub> and Mo3*d*<sub>3/2</sub> of pr-10MoO<sub>3</sub>-SnO<sub>2</sub>(5) were 232 and 235.2 eV, respectively. Comparison of these values with standard ones reported in a literature [19] showed that they may correspond to Mo<sup>5+</sup> ions.

### **3.2 Gas-sensing properties of pr-SnO<sub>2</sub>(*n*) and pr-*m*MoO<sub>3</sub>-SnO<sub>2</sub>(*n*) sensors**

Figure 11 shows a SEM image of surface of a pr-5MoO<sub>3</sub>-SnO<sub>2</sub>(5) sensor. The morphology is well-developed porous structure with clear boundaries among submicron-size porous SnO<sub>2</sub> particles, which were hardly destroyed during the

fabrication process of the thick film. The morphology of other sensors was also similar to this sensor.

Figures 12 and 13 show temperature dependence of response to 5 ppm NO<sub>2</sub> in air of all samples. Almost all samples showed the largest NO<sub>2</sub> response at 300°C, except for pr-10MoO<sub>3</sub>-SnO<sub>2</sub>(3). The excellent NO<sub>2</sub>-response behavior of pr-*m*MoO<sub>3</sub>-SnO<sub>2</sub>(*n*) can be understood from the following equation using Kröger-Vink notation:



Therefore, according to the eq. 1, the increase in the adsorbed amount of NO<sub>2</sub> (negatively charged chemisorptions) is due to the increased concentration of electrons. It seems that an increase in the amount of Mo content leads to a significant increase of electrons and surface area and consequently an increase in sensor response. Therefore, the higher response at lower operating temperature of pr-10MoO<sub>3</sub>-SnO<sub>2</sub>(3) sensor can be explained on the basis of high surface area and acidic nature of film. In addition, pr-10MoO<sub>3</sub>-SnO<sub>2</sub>(5) film is more sensitive to NO<sub>2</sub> gas in comparison to other pr-*m*MoO<sub>3</sub>-SnO<sub>2</sub>(5). Since the SSA of pr-10MoO<sub>3</sub>-SnO<sub>2</sub>(5) is smaller than those of other pr-*m*MoO<sub>3</sub>-SnO<sub>2</sub>(5), the higher response of pr-10MoO<sub>3</sub>-SnO<sub>2</sub>(5) can be related to the amount of Mo species. Also, pr-*m*MoO<sub>3</sub>-SnO<sub>2</sub>(3) films show relatively higher

response than  $\text{pr-}m\text{MoO}_3\text{-SnO}_2(5)$  films, probably because of larger surface area compared with that of  $\text{pr-}m\text{MoO}_3\text{-SnO}_2(5)$  powders.

Figure 14 shows response transients of  $\text{pr-SnO}_2(3)$  and  $\text{pr-}m\text{MoO}_3\text{-SnO}_2(3)$  samples at  $350^\circ\text{C}$ . The recovery speed was slower with increasing the amount of  $\text{MoO}_3$ , probably due to slow desorption of  $\text{NO}_2^-$  and  $\text{NO}_3^-$  species which strongly bonded with molybdenum species on the surface. In addition, the resistance in air of all sensors was terribly high, probably due to the small grain size as well as a little number of boundaries among their submicron-size porous particles

Figures 15 and 16 show temperature dependence of responses to 100 ppm  $\text{C}_2\text{H}_5\text{OH}$ , 1000 ppm  $\text{H}_2$  and 5 ppm  $\text{NO}_2$  of  $\text{pr-}l\text{MoO}_3\text{-SnO}_2(n)$  and  $\text{pr-SnO}_2(n)$  sensors, respectively. The addition of  $\text{MoO}_3$  improved the sensor response and selectivity to  $\text{NO}_2$  gas. Among them,  $\text{pr-}l\text{MoO}_3\text{-SnO}_2(3)$  sensor showed large response to  $\text{NO}_2$  and excellent selectivity to  $\text{NO}_2$  at a low operating temperature of  $250^\circ\text{C}$ , as shown in Figure 15(a). On the other hand, Figure 15(b) showed that  $\text{pr-}l\text{MoO}_3\text{-SnO}_2(5)$  sensor showed large response to ethanol at higher temperature ( $400^\circ\text{C}$ ) and large response to  $\text{NO}_2$  gas at lower temperatures ( $300^\circ\text{C}$ ).

On the other hand,  $\text{pr-SnO}_2(n)$  sensors showed extremely large response to ethanol in comparison to other gases, as shown in Fig. 16. It shows that the presence of many acidic centers on the surface of thick films can reduce the sensor response to ethanol, because the ethanol conversion takes place with dehydration route [21]. It seems that the presence of molybdenum species at the  $\text{SnO}_2$  nano- and meso-porous structures changes their acidity performance which varies its reactivity versus certain gas species.

#### **4. Conclusion**

$\text{pr-SnO}_2(n)$  and  $\text{pr-}m\text{MoO}_3\text{-SnO}_2(n)$  powders with well-developed nano- and meso-porous structures have been synthesized by an ultrasonic spray-pyrolysis method. The results revealed that the use of PMMA microspheres as a template and the doping of  $\text{MoO}_3$  affected on the structural, morphological and sensing properties of  $\text{SnO}_2$  powders. The nano- and meso-porous  $\text{SnO}_2$  powders were obtained by adding 3 and 5 g of PMMA microspheres in the precursor solution, respectively. Also, the addition of 5 g PMMA microspheres accelerated segregation of  $\text{MoO}_3$  from the  $\text{SnO}_2$  lattice. Namely,  $\text{MoO}_3$  particles were separately formed among  $\text{SnO}_2$  crystallites of  $\text{pr-}m\text{MoO}_3\text{-SnO}_2(5)$  and then the surface area decreased. This phenomenon was confirmed by BET, TEM

and EDX. On the other hand, the MoO<sub>3</sub>-doping to pr-SnO<sub>2</sub>(*n*) improved the sensor response and selectivity towards NO<sub>2</sub> gas. This sensing behavior was well-correlated with the increase in acidity of the surface of the SnO<sub>2</sub> caused by the presence of molybdenum species in the SnO<sub>2</sub> nano- and meso-porous structures.

**Acknowledgment:**

One of the authors (A. Anaraki Firooz) would like to acknowledge the sabbatical leave awarded by the Ministry of Science and Technology of the Islamic Republic of Iran.



## Reference

- [1] A. A. Firooz, A. R. Mahjoub, A. A. Khodadadi, Effects of flower-like, sheet-like and granular SnO<sub>2</sub> nanostructures prepared by solid-state reactions on CO sensing, *Mat. Chem. Phys* 115 (2009) 196–199.
- [2] A. A. Firooz, A. R. Mahjoub, A. A. Khodadadi, Highly sensitive CO and ethanol nanoflower-like SnO<sub>2</sub> sensor among various morphologies obtained by using single and mixed ionic surfactant templates, *Sens. Actuators B: Chem*, 141 (2009) 89–96.
- [3] A. A. Firooz, A. R. Mahjoub, A. A. Khodadadi, Preparation of SnO<sub>2</sub> nanoparticles and nanorods by using a hydrothermal method at low temperature, *Mater. Lett.* 62 (2008) 1789-1792.
- [4] Z. Wen, G. Wang, W. Lu, Q. Wang, Q. Zhang, J. Li, Enhanced Photocatalytic Properties of Mesoporous SnO<sub>2</sub> Induced by Low Concentration ZnO Doping, *Cryst. Growth Des*, 7 (2007) ,1722-1725.
- [5] Y-H. Choi, M. Yang, S-H Hong, H<sub>2</sub> sensing characteristics of highly textured Pd-doped SnO<sub>2</sub> thin films, *Sens. Actuators B: Chem*, 134 (2008) 117–121.
- [6] J. H. Pan, S. Y. Chai, C. Lee, S-E. Park, W. I. Lee, Controlled Formation of Highly Crystallized Cubic and Hexagonal Mesoporous SnO<sub>2</sub> Thin Films, *J. Phys. Chem. C* 2007, 111, 5582-5587.

- [7] Sun, J. Q.; Wang, J. S.; Wu, X. C.; Zhang, G. S.; Wei, J. Y.; Zhang, S. Q.; Li, H.; Chen, D. R. Novel Method for High-Yield Synthesis of Rutile SnO<sub>2</sub> Nanorods by Oriented Aggregation Cryst. Growth Des. 2006, 6, 1584-1587.
- [8] T. Hyodo, K. Sasahara, Y. Shimizu, M. Egashira, Preparation of macroporous SnO<sub>2</sub> films using PMMA microspheres and their sensing properties to NO<sub>x</sub> and H<sub>2</sub>, Sens. Actuators B: Chem, 106 (2005) 580–590.
- [9] Z.A. Ansari, S.G. Ansari, T. Ko, J.-H. Oh, Effect of MoO<sub>3</sub> doping and grain size on SnO<sub>2</sub>-enhancement of sensitivity and selectivity for CO and H<sub>2</sub> gas sensing, Sens. Actuators B: Chem, 87 (2002) 105–114.
- [10] X. Jiaqiang, W. Ding, Q. Lipeng, Y. Weijun, P. Qingyi, SnO<sub>2</sub> nanorods and hollow spheres: Controlled synthesis and gas sensing properties, Sens. Actuators B: Chem, 137 (2009) 490–495.
- [11] J. Kaur, V.D. Vankar, M.C. Bhatnagar, Effect of MoO<sub>3</sub> addition on the NO<sub>2</sub> sensing properties of SnO<sub>2</sub> thin films, Sens. Actuators B: Chem, 133 (2008) 650–655.
- [12] E. Zampiceni, E. Bontempi, G. Sberveglieri, L. E. Depero, Mo influence on SnO<sub>2</sub> thin films properties, Thin Solid Films, 418 (2002) 16–20.

- [13] J. Arbiol, J.R. Morante, P. Bouvier, T. Pagnier, E.A. Makeeva, M.N. Rumyantseva, A.M. Gaskov, SnO<sub>2</sub>/MoO<sub>3</sub>-nanostructure and alcohol detection, *Sens. Actuators B: Chem*, 118 (2006) 156–162.
- [14] K. Hieda, T. Hyodo, Y. Shimizu, M. Egashira, Preparation of porous tin dioxide powder by ultrasonic spray pyrolysis and their application to sensor materials, *Sens. Actuators B: Chem*, 133 (2008) 144–150.
- [15] F. Harb, B. Gerand, G. Nowogrocki, M. Figlarz, Structural filiation between a newmolybdenum oxide hydrate (MoO<sub>3</sub>·(1/3)H<sub>2</sub>O) and a newmonoclinic form of MoO<sub>3</sub> obtained by dehydration, *Solid State Ionics* 32-33 (I) (1989) 84–90.
- [16] S.G. Ansari, M.A. Dar, Y-S. Kim, G-S. Kim, H-K. Seo, G. Khang, H-S. Shin, Effect of growth temperature on the morphology and bonded states of SnO<sub>2</sub> nanobaskets, *Applied Surface Science* 253 (2007) 4668–4672.
- [17] B. Mirkelamoglu, G. Karakas, The role of alkali-metal promotion on CO oxidation over PdO/SnO<sub>2</sub> catalysts, *Applied Catalysis A: General*, 299 (2006) 84–94.
- [18] C.D. Wagner, W.M. Riggs. L.E. Davis, J.F. Moulder, G.E. Muilenberg, *Handbook of X-ray Photoelectron Spectroscopy*, Physical Electronics Division, Perkin-Elmer, Eden Prairie, Minnesota, 1979.

- [19] Y. Zhang, J. Yuan, Y. Cao, L. Song, X. Hu, Photochromic behavior of Li-stabilized MoO<sub>3</sub> sol–gels, *Journal of Non-Crystalline Solids* 354 (2008) 1276–1280.
- [20] A. Chiorino, G. Ghiotti, F. Prinetto, M.C. Carotta, D. Gnani, G. Martinelli, Preparation and characterization of SnO and MoO –SnO nanosized powders for thick film gas sensors, *Sens. Actuators B: Chem*, 58 (1999) 338–349.
- [21] N. Yamazoe, G. Sakai, K. Shimano, Oxide semiconductor gas sensors, *Catalysis Surveys from Asia*, 7 (2003) 63-75.

## **Biographies**

**A. Anaraki Firooz** received MSc degrees in Inorganic Chemistry from Tarbiat Modares University in 2005. She is a PhD student at the Department of Chemistry under the supervisions of Prof. A. R. Mahjoub and Prof. A. A. Khodadadi. Her research project focuses on "The effect of morphology and additives on sensing and catalytic functions of SnO<sub>2</sub> nanostructures". She is now a visiting researcher in Nagasaki University.

**T. Hyodo** received his B. Eng. Degree in applied chemistry and M. Eng. Degree in materials science and technology in 1992 and 1994, respectively, and Dr. Eng. Degree in 1997 from Kyushu University. He has been an Assistant Professor at Nagasaki University since 2007. His research interests are the developments of electrochemical devices such as chemical sensors and lithium batteries, and mesoporous and macroporous materials.

**A. R. Mahjoub** received his MS in Organic chemistry in 1988 and his PhD in Inorganic chemistry in 1993 from University of Berlin, Germany. His research activity covers many aspects of the synthesis, characterization and chemical –physics of metal oxides and nanooxides with particular emphasis to catalytic and photo degradation properties.

**A. Khodadadi** received his MS in Chemical Engineering from the University of Tehran in 1986 and his PhD in Catalysis and Reaction Engineering from University of Waterloo, Canada, in 1994. His research interests include catalysis, reaction engineering, and nanostructured materials as applied to nanoparticles, carbon nanotubes, plasma-catalytic conversion of natural gas to liquids and chemicals, metal oxide semiconductor gas sensors, air pollution control using catalytic converters and oxygen sensors using solid electrolytes.

**Y. Shimizu** received his B. Eng. Degree in applied chemistry in 1980 and Dr. Eng. Degree in 1987 from Kyushu University. He has been a Professor at Nagasaki University since 2005. His current research concentrates on development of odor sensors and design of intelligent sensors by controlling gas diffusivity and reactivity.

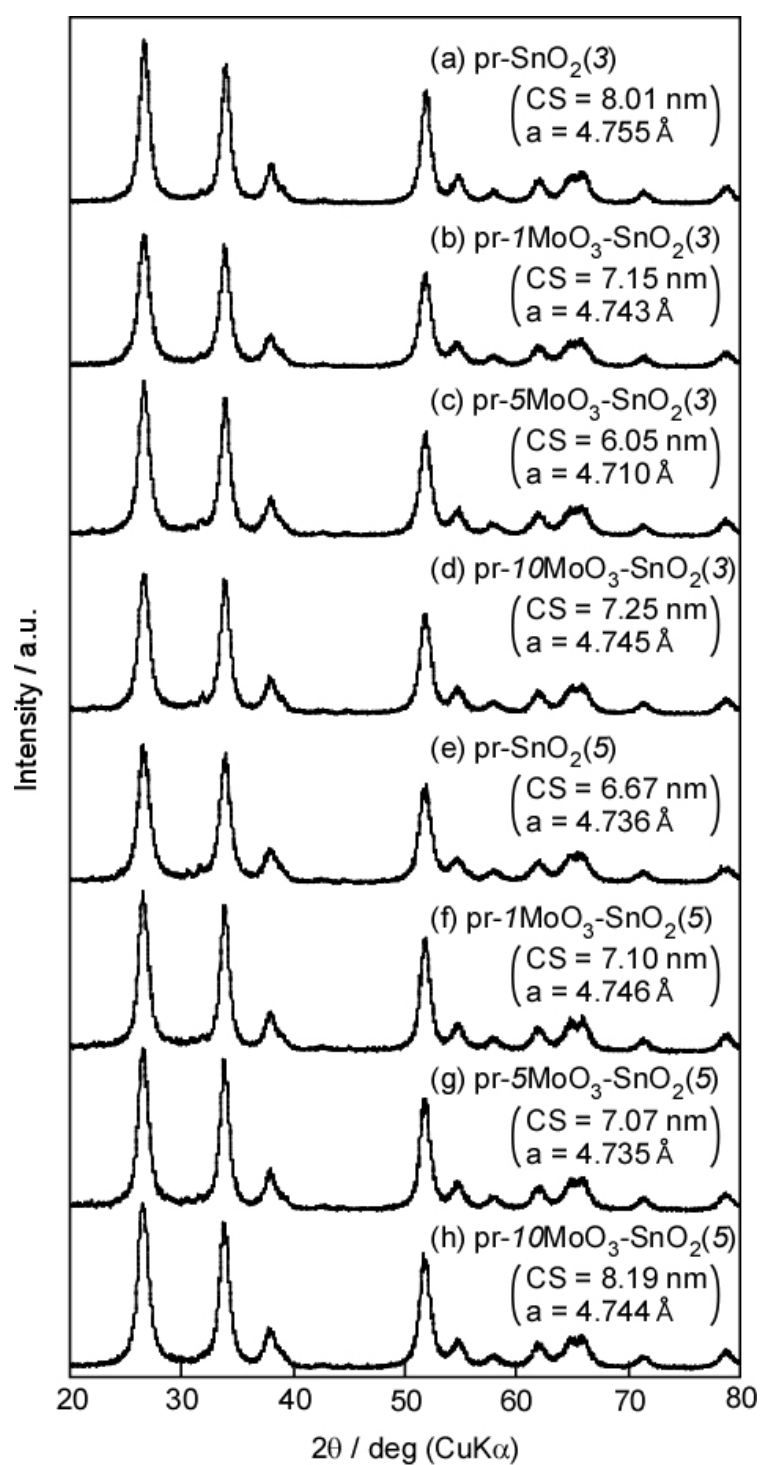


Figure 1: XRD patterns of a) pr-SnO<sub>2</sub>(3), b-d) pr-*m*MoO<sub>3</sub>-SnO<sub>2</sub>(3), e) pr-SnO<sub>2</sub>(5) and f-h) pr-*m*MoO<sub>3</sub>-SnO<sub>2</sub>(5) powders (*m* = 1, 5 and 10), along with their crystallite size(CS) and lattice parameter (a).

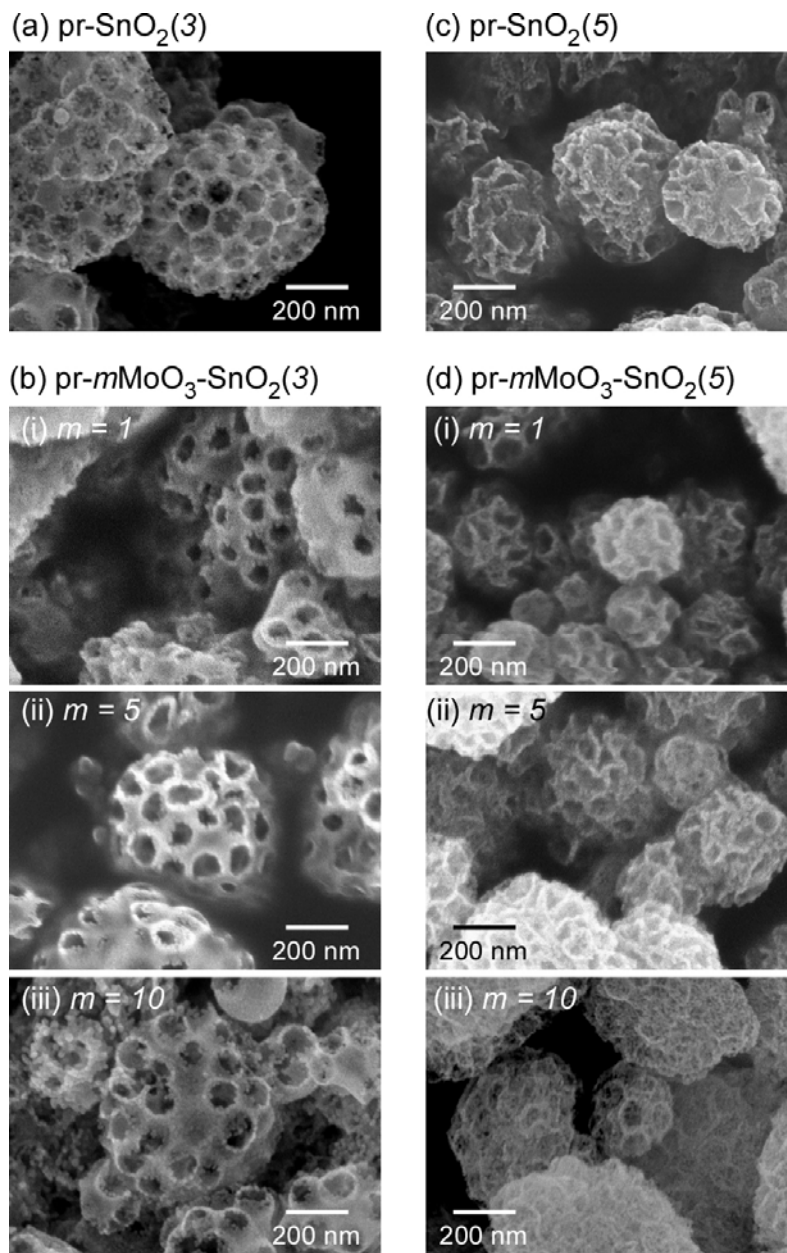


Figure 2: SEM images of (a) pr-SnO<sub>2</sub>(3), (b) pr-*m*MoO<sub>3</sub>-SnO<sub>2</sub>(3), (c) pr-SnO<sub>2</sub>(5) and (d) pr-*m*MoO<sub>3</sub>-SnO<sub>2</sub>(5) powders.

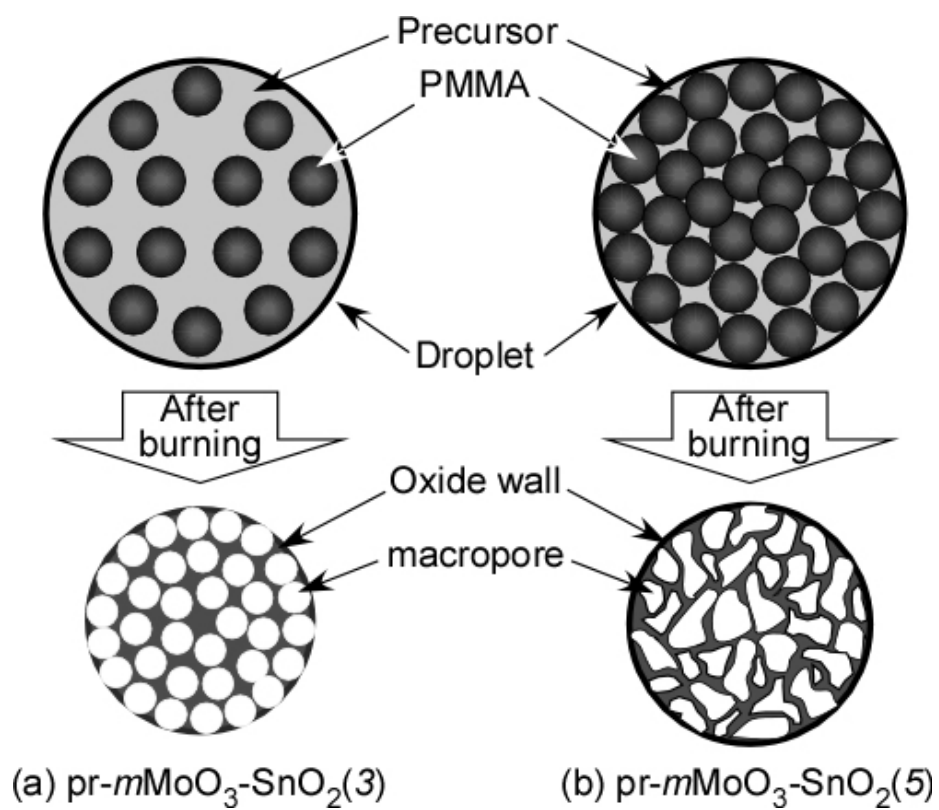


Figure 3: Schematic drawing of formation mechanism of pores in a) pr- $m\text{MoO}_3$ - $\text{SnO}_2(3)$  and b) pr- $m\text{MoO}_3$ - $\text{SnO}_2(5)$ .



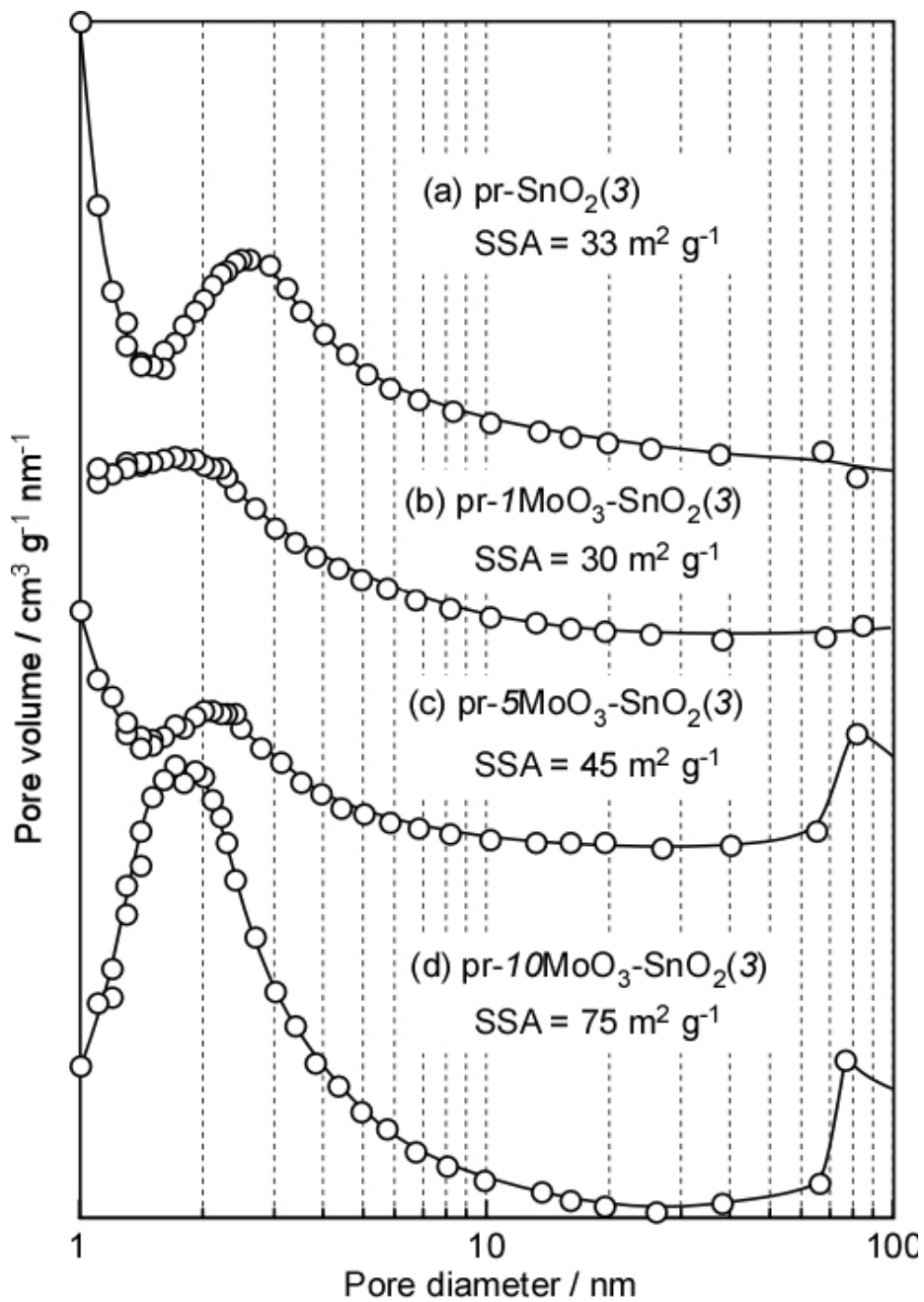


Figure 4: Pore size distributions of  $\text{pr-SnO}_2(3)$  and  $\text{pr-}m\text{MoO}_3\text{-SnO}_2(3)$  powders, along with their SSA.

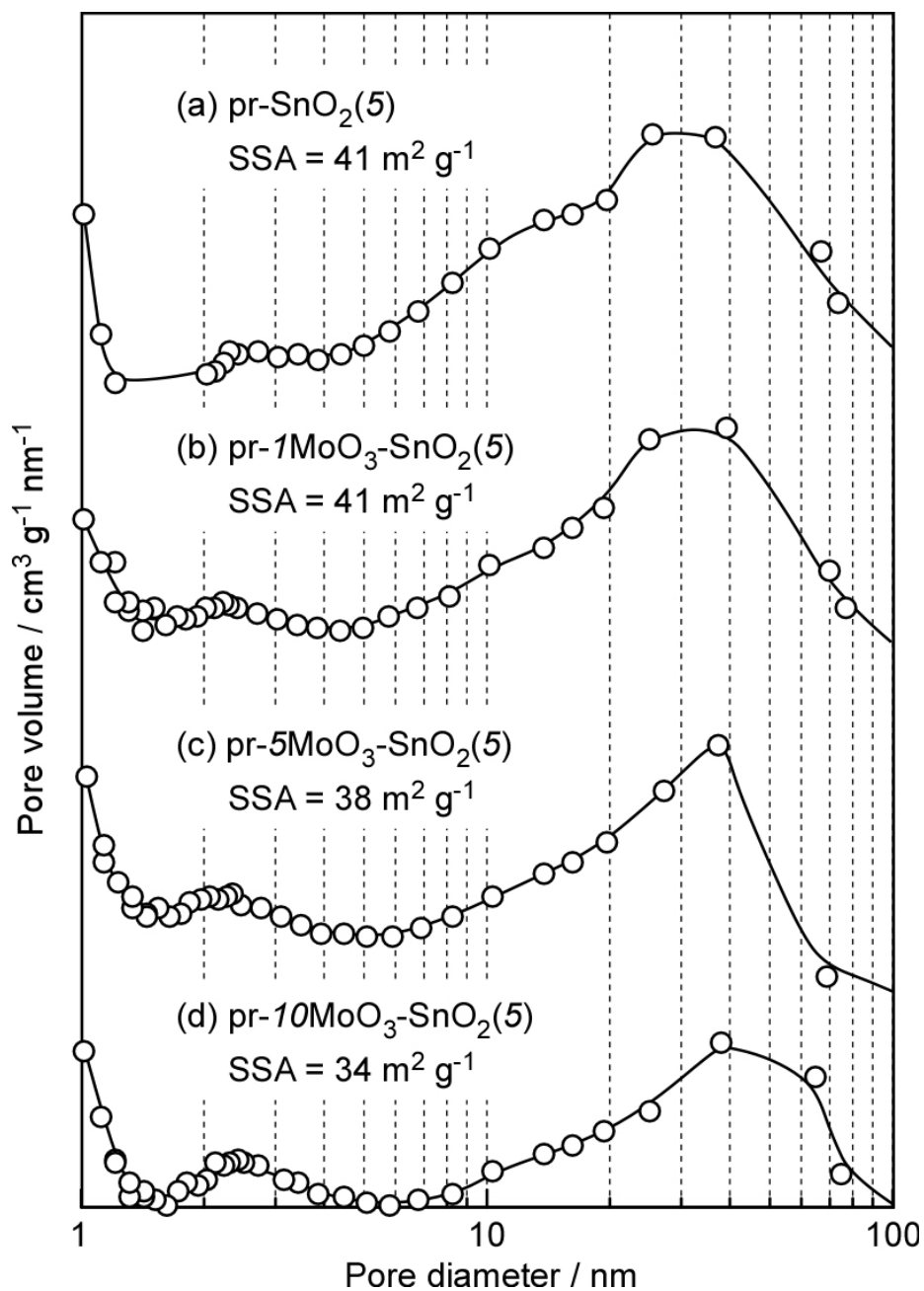


Figure 5: Pore size distributions of pr- $\text{SnO}_2(5)$  and pr- $m\text{MoO}_3\text{-SnO}_2(5)$  powders, along with their SSA.

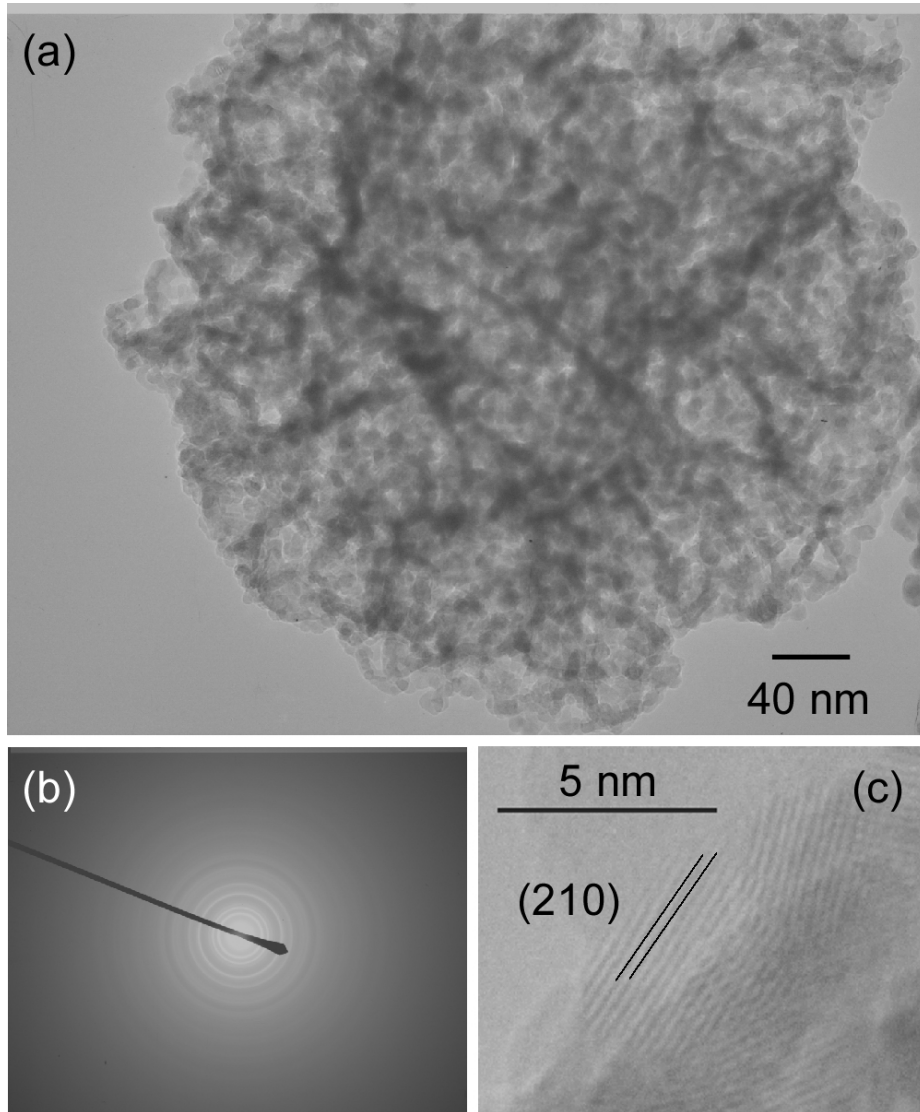


Figure 6: a) TEM image, b) SAED pattern and c) high-resolution transmission electron micrograph of pr-SnO<sub>2</sub>(5).

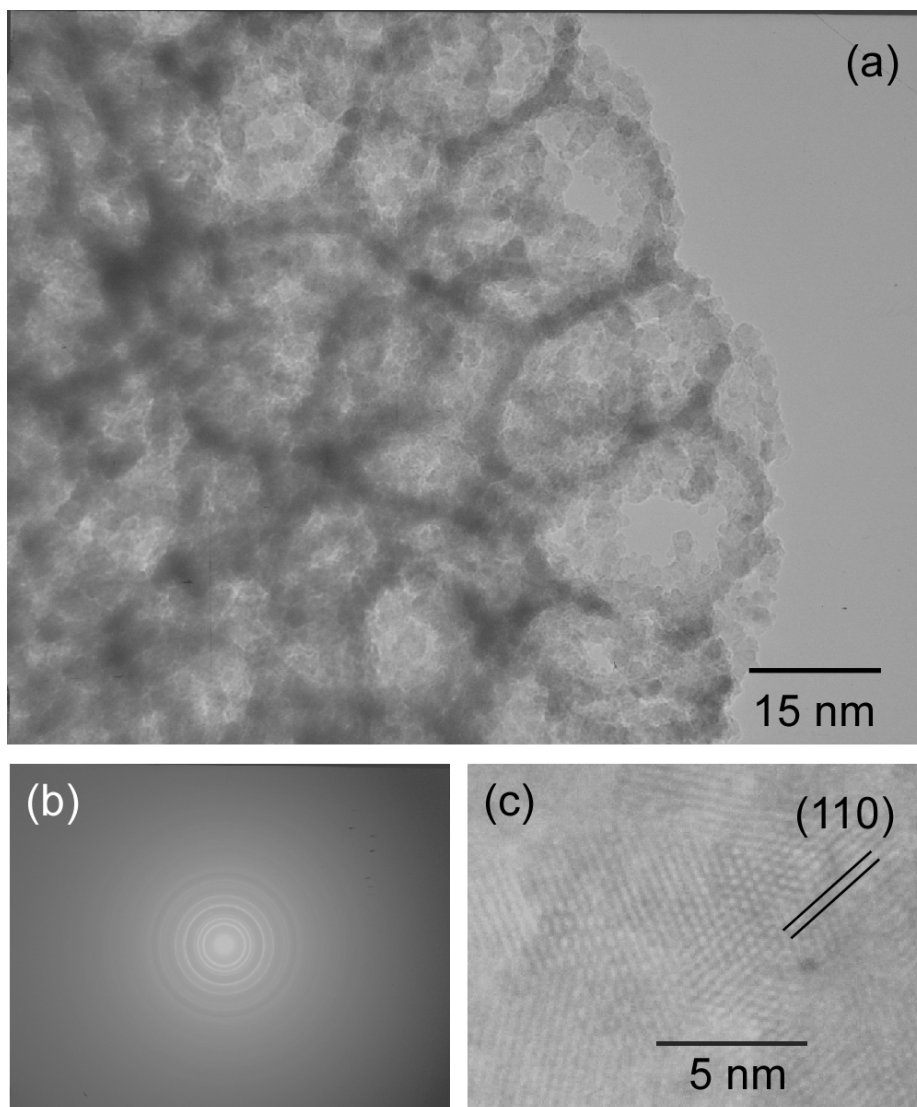


Figure 7: a) TEM image, b) SAED pattern and c) high-resolution transmission electron micrograph of  $pr\text{-}10\text{MoO}_3\text{-SnO}_2(3)$ .

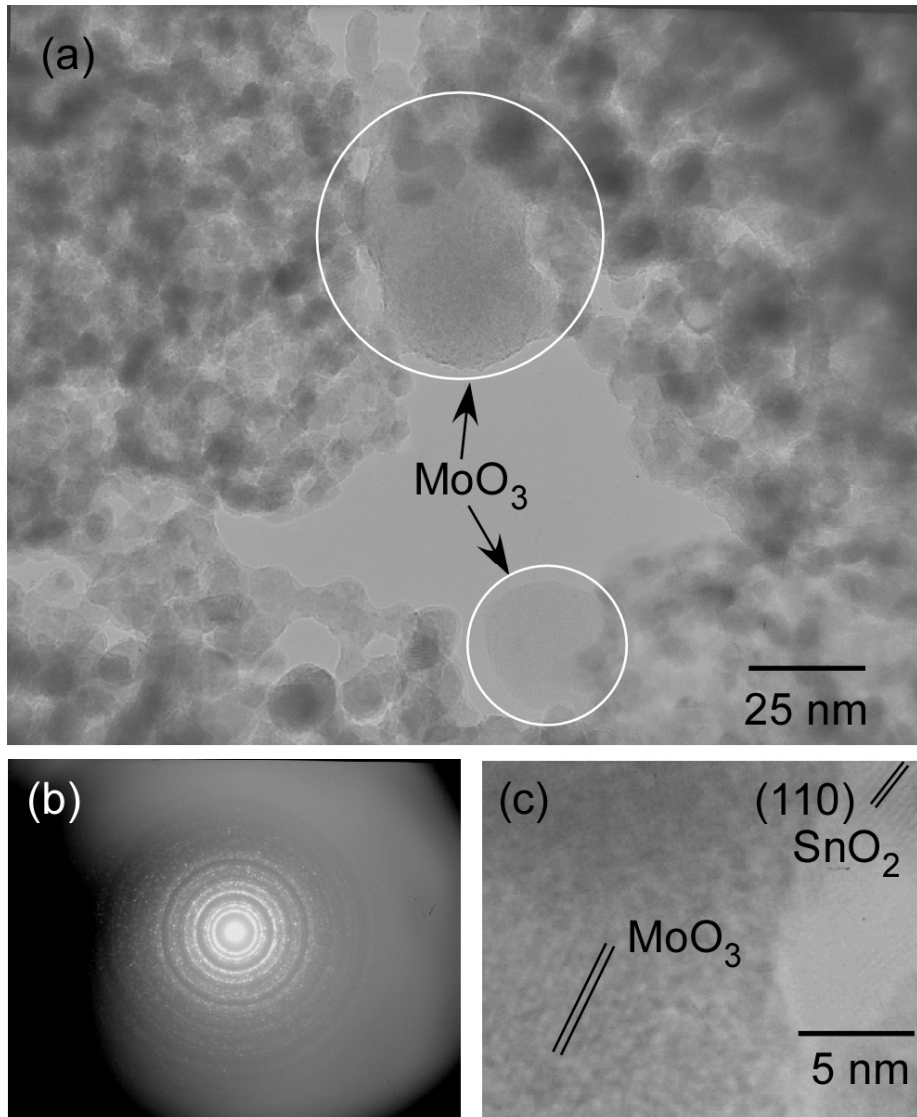


Figure 8: a) TEM image, b) SAED pattern and c) high-resolution transmission electron micrograph of pr-10MoO<sub>3</sub>-SnO<sub>2</sub>(5).

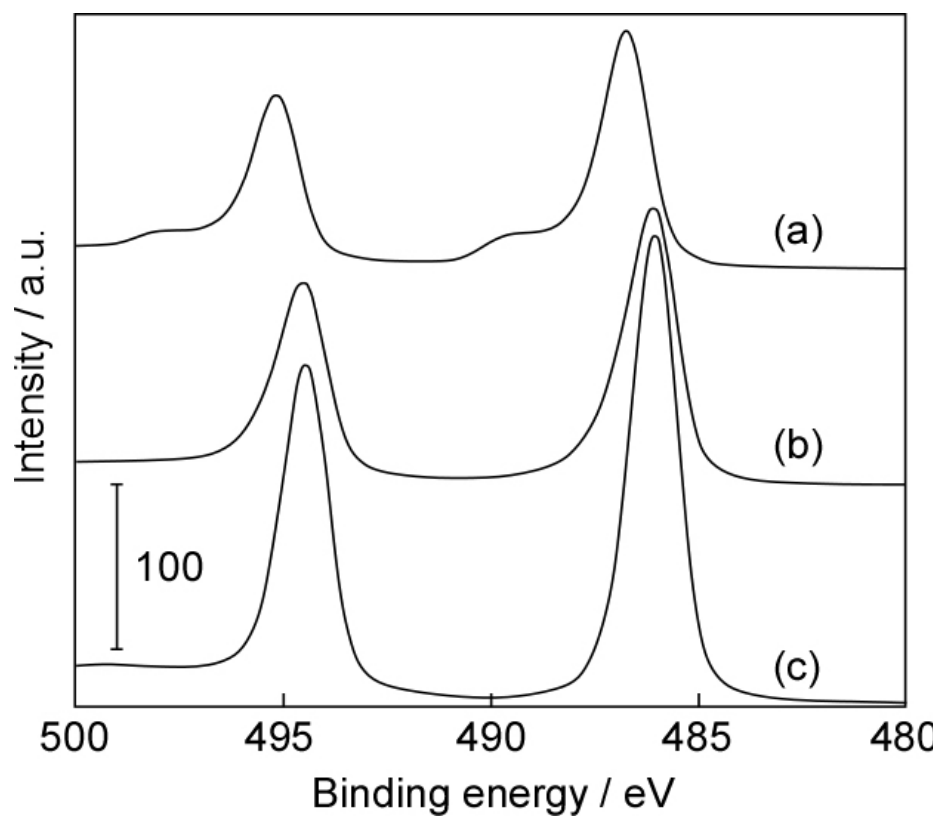


Figure 9: XPS spectra of Sn3d for pr-10MoO<sub>3</sub>-SnO<sub>2</sub>(n) a) n=3 b) n=5, and c) pr-SnO<sub>2</sub>(5).

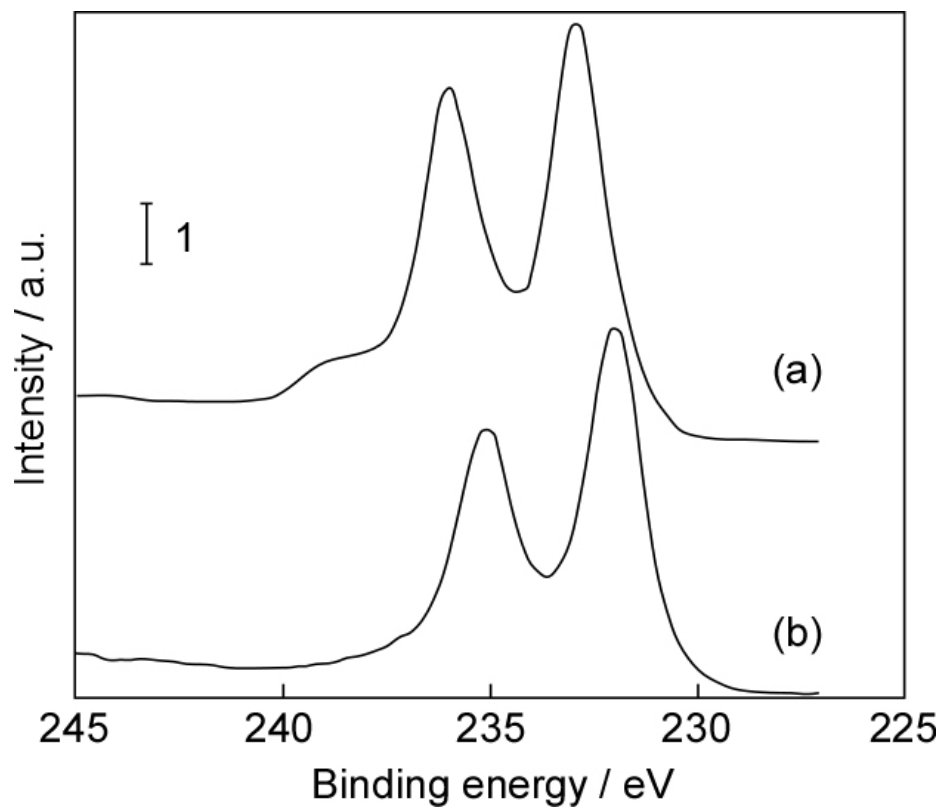


Figure 10: XPS spectra of Mo3d for pr-10MoO<sub>3</sub>-SnO<sub>2</sub>(n) a)  $n=3$ , and b)  $n=5$ .

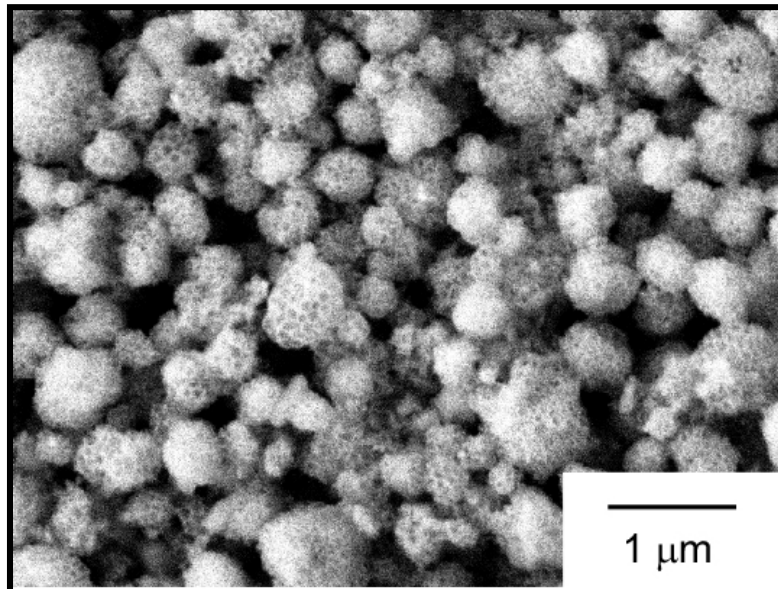


Figure 11: SEM image of a pr-5MoO<sub>3</sub>-SnO<sub>2</sub>(5) thick film.



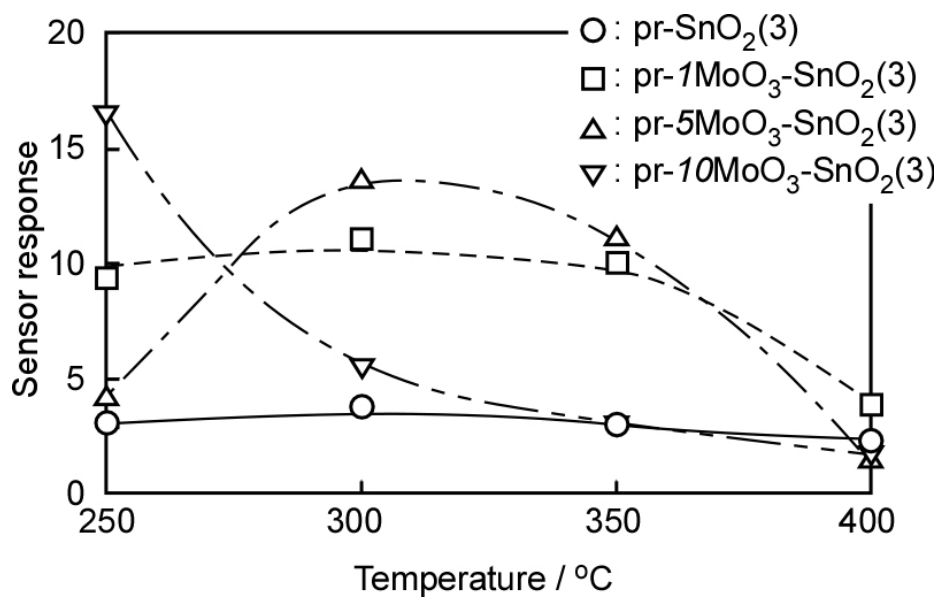


Figure 12: Temperature dependence of response of pr-SnO<sub>2</sub>(3) and pr-*m*MoO<sub>3</sub>-SnO<sub>2</sub>(3) (*m* = 1, 5 and 10) thick films to 5 ppm NO<sub>2</sub>.

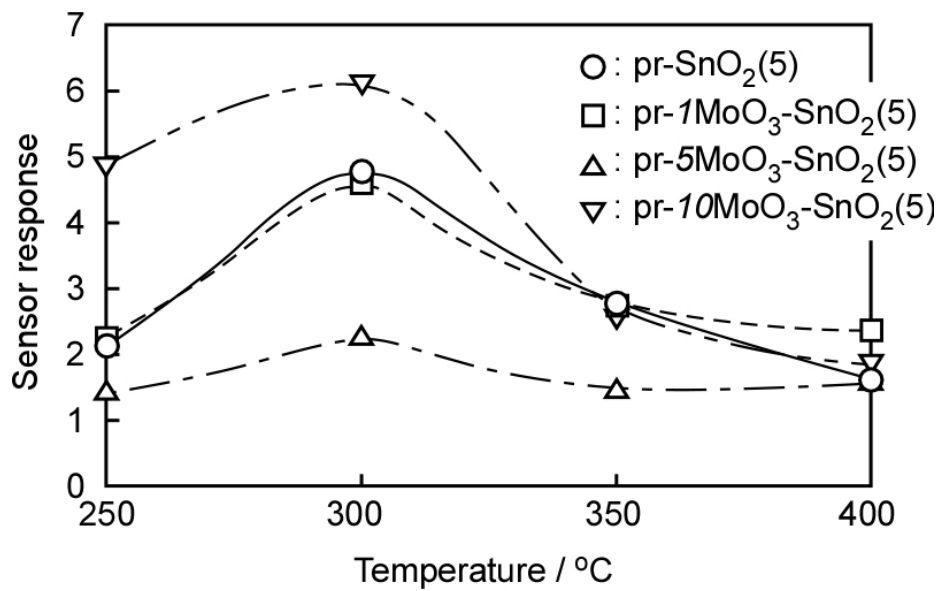


Figure 13: Temperature dependence of response of pr-SnO<sub>2</sub>(5) and pr-*m*MoO<sub>3</sub>-SnO<sub>2</sub>(5) (*m* = 1, 5 and 10) thick films to 5 ppm NO<sub>2</sub>.

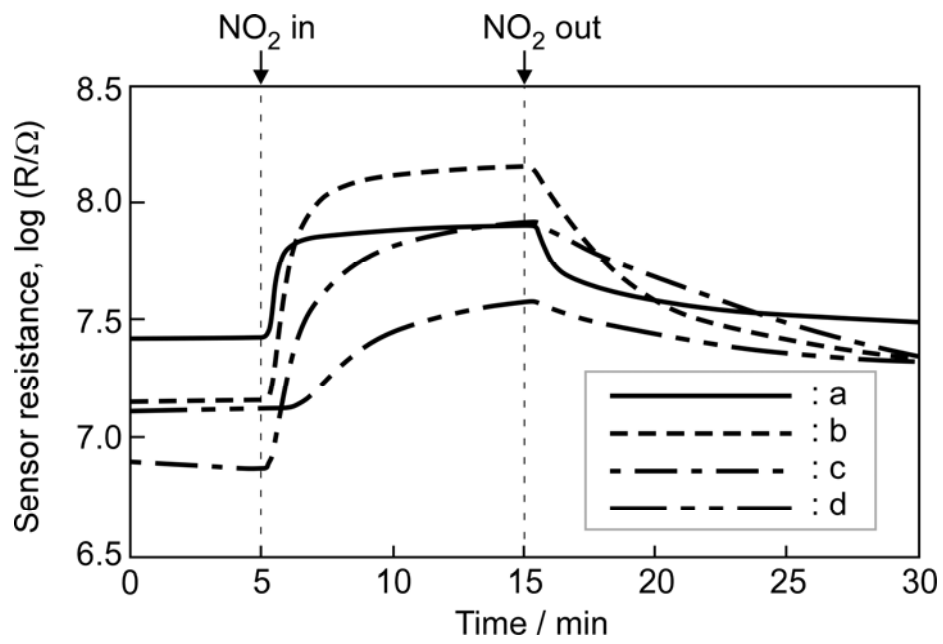


Figure 14: Response transients of thick films of a)  $\text{pr-SnO}_2(3)$ , b-d)  $\text{pr-}m\text{MoO}_3\text{-SnO}_2(3)$  powders ( $m = 1, 5$  and  $10$ ), respectively.

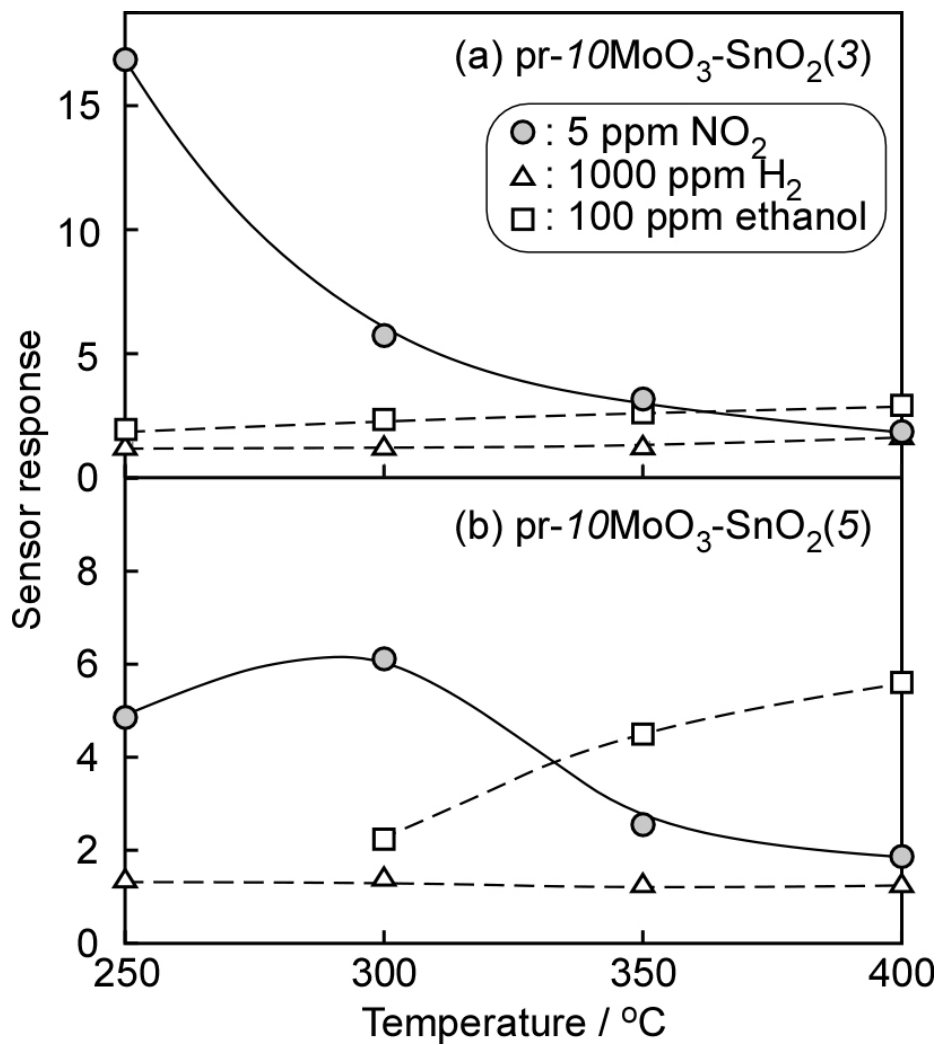


Figure 15: Temperature dependence of response of pr-10MoO<sub>3</sub>-SnO<sub>2</sub>(3) and pr-10MoO<sub>3</sub>-SnO<sub>2</sub>(5) sensors.

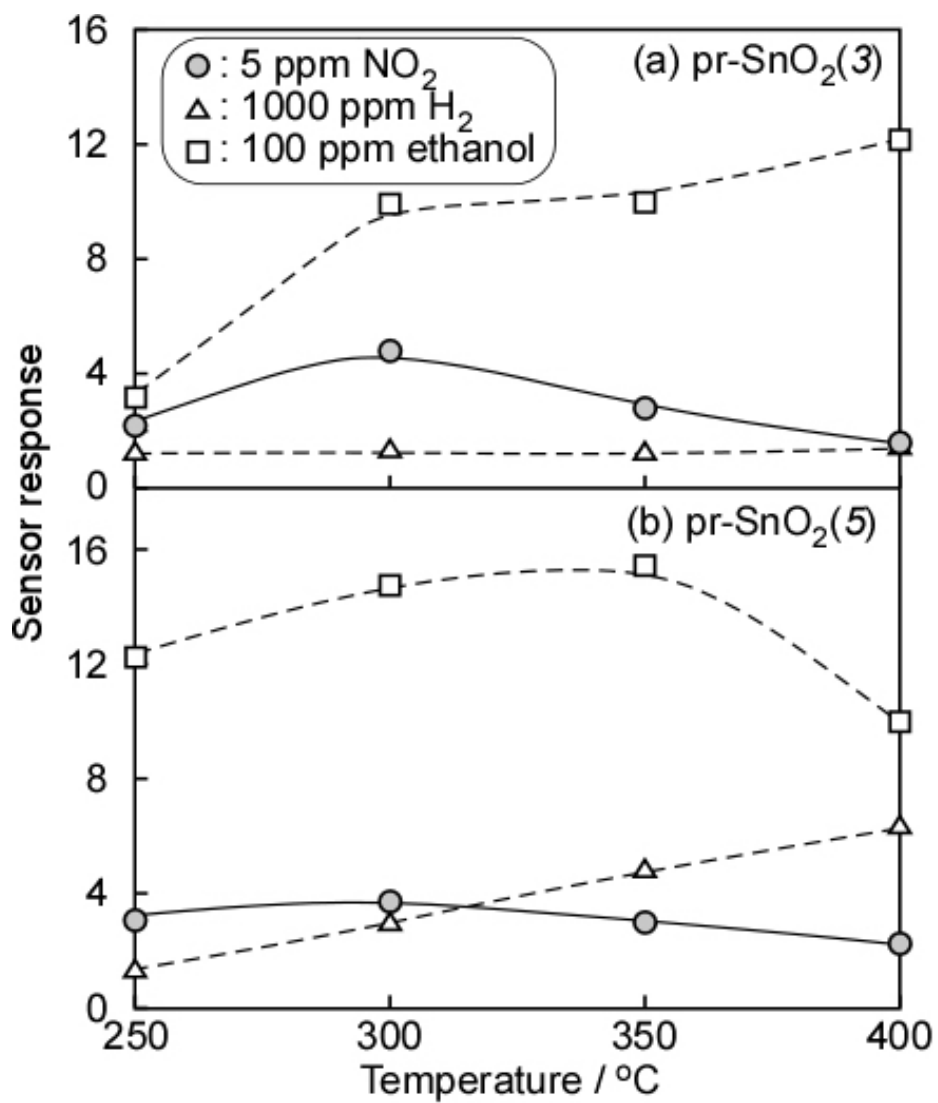


Figure 16: Temperature dependence of response of pr-SnO<sub>2</sub>(3) and pr-SnO<sub>2</sub>(5) sensors.